

Simultaneous Retrievals of Nighttime O(3P) and Total OH Densities From Satellite Observations of Meinel Band Emissions

Peter A. Panka, Alexander A. Kutepov, Yajun Zhu, Martin Kaufmann, Konstantinos S. Kalogerakis, Ladislav Rezac, Artem G. Feofilov, Daniel R. Marsh, Diego Janches

▶ **To cite this version:**

Peter A. Panka, Alexander A. Kutepov, Yajun Zhu, Martin Kaufmann, Konstantinos S. Kalogerakis, et al.. Simultaneous Retrievals of Nighttime O(3P) and Total OH Densities From Satellite Observations of Meinel Band Emissions. Geophysical Research Letters, 2021, 48, 10.1029/2020GL091053 . insu-03726962

HAL Id: insu-03726962

https://insu.hal.science/insu-03726962

Submitted on 19 Aug 2022

HAL is a multi-disciplinary open access archive for the deposit and dissemination of scientific research documents, whether they are published or not. The documents may come from teaching and research institutions in France or abroad, or from public or private research centers.

L'archive ouverte pluridisciplinaire **HAL**, est destinée au dépôt et à la diffusion de documents scientifiques de niveau recherche, publiés ou non, émanant des établissements d'enseignement et de recherche français ou étrangers, des laboratoires publics ou privés.

Copyright

Check for updates

AGU ADVANCING EARTH AND SPACE SCIENCE

Geophysical Research Letters

RESEARCH LETTER
10.1029/2020GL091053

Simultaneous Retrievals of Nighttime O(^{3}P) and Total OH Densities From Satellite Observations of Meinel Band Emissions

Peter A. Panka[1], Alexander A. Kutepov[1,2], Yajun Zhu[3], Martin Kaufmann[4,5], Konstantinos S. Kalogerakis[6], Ladislav Rezac[7], Artem G. Feofilov[8], Daniel R. Marsh[9,10], and Diego Janches[1]

[1]NASA Goddard Space Flight Center, Greenbelt, MD, USA, [2]The Catholic University of America, Washington, DC, USA, [3]State Key Laboratory of Space Weather, National Space Science Center, Chinese Academy of Sciences, Beijing, China, [4]Institute of Energy and Climate Research, Forschungszentrum Jülich, Jülich, Germany, [5]Institute for Atmospheric and Environmental Research, University of Wuppertal, Wuppertal, Germany, [6]Center for Geospace Studies, SRI International, Menlo Park, CA, USA, [7]Max-Planck-Institut für Sonnensystemforschung, Göttingen, Germany, [8]LMD/IPSL, Sorbonne Université, UPMC Univ Paris 06, CNRS, École polytechnique, Palaiseau, France, [9]National Center for Atmospheric Research, Boulder, CO, USA, [10]Faculty of Engineering and Physical Sciences, University of Leeds, Leeds, UK

Key Points:

- A novel approach to the simultaneous retrieval of nighttime O(^{3}P) and OH densities from space-based satellite observations is presented
- Total OH densities are retrieved for the first time in the mesosphere and lower thermosphere (MLT)
- Scanning Imaging Absorption spectroMeter for Atmospheric CHartographY retrieved OH densities are comparable to chemical models in the MLT while Sounding of the Atmosphere using Broadband Emission Radiometry retrieved OH densities are higher

Correspondence to:
P. A. Panka,
peter.a.panka@nasa.gov

Citation:
Panka, P. A., Kutepov, A. A., Zhu, Y., Kaufmann, M., Kalogerakis, K. S., Rezac, L., et al. (2021). Simultaneous retrievals of nighttime O(^{3}P) and total OH densities from satellite observations of Meinel band emissions. *Geophysical Research Letters*, *48*, e2020GL091053. https://doi.org/10.1029/2020GL091053

Received 2 OCT 2020
Accepted 23 NOV 2020

Abstract Retrieving the total number density [OH], which is used in the chemical balance equations and is the sum of both ground and excited vibrational state populations, is a challenging problem to such a degree there exist no such estimates from recent space observations. We present a novel retrieval approach to simultaneously and self-consistently derive both [O(^{3}P)] and total [OH] in the nighttime mesosphere and lower thermosphere which operates with the Meinel band volume emission rates and their ratios. Its application to the Sounding of the Atmosphere using Broadband Emission Radiometry (SABER) and Scanning Imaging Absorption spectroMeter for Atmospheric CHartographY (SCIAMACHY) observations shows a good agreement of the retrieved [O(^{3}P)] taking into account the measurement uncertainties and variation of model inputs used. However, retrieved [OH] show a large discrepancy, mainly above 90 km. SCIAMACHY [OH] is generally in good agreement with WACCM [OH] after accounting for uncertainties, while SABER OH is larger than WACCM [OH] by up to a factor of 2.

Plain Language Summary The hydroxyl molecule plays an important role in the physics, chemistry, and dynamics of the middle and upper atmosphere region (60–120 km). Obtaining total hydroxyl density from its molecular emissions is a challenging problem to such a degree there exist no such estimates from the recent space observations. We present a novel approach to obtain both atomic oxygen and total hydroxyl densities in the middle and upper atmosphere from nighttime observations of the hydroxyl molecular emissions. We apply the new approach to two different space-based instrument observations of hydroxyl emissions at multiple infrared wavelengths. The atomic oxygen densities obtained from the two instruments using our new approach are in good agreement after taking into account uncertainties, while the hydroxyl densities show a large discrepancy.

1. Introduction

The hydroxyl radical (OH) plays a fundamental role in the chemistry and dynamics of the middle and upper atmosphere. The measured OH rotational-vibrational line emissions are used to derive kinetic temperature and observe dynamical processes such as tides, planetary, and gravity waves (Grygalashvyly et al., 2014 and references therein). Moreover, as was recently shown by Sharma et al. (2015) and Kalogerakis et al. (2016), collisions between OH and O(^{3}P) provide a nighttime source of O(^{1}D). Therefore, detailed knowledge of [OH] and its variability is crucially important in understanding the formation of different types of airglow and infrared emissions (Kalogerakis, 2019; Panka et al., 2017) of the nighttime mesosphere.

The emissions of nighttime mesospheric OH were measured by various instruments in a number of spectral ranges. Pickett et al. (2006) used the Microwave Limb Sounder instrument on the Aura satellite measurements of the thermal emission from 2.5 THz rotational lines to retrieve the altitude profile from 18-94 km of

© 2020. American Geophysical Union. All Rights Reserved.

the ground vibrational state OH($v = 0$) density. Cosby and Slanger (2007) used the Echelle Spectrograph and Imager on the Keck II telescope at Mauna Kea to measure emission intensities of 16 OH Meinel bands in the spectral range 0.4–1.06 μm which were converted into the OH(v) column densities from $v = 3$–9. Migliorini et al. (2015) analyzed the Visible and Infrared Thermal Imaging Spectrometer (VIRTIS) measurements on board the Rosetta mission. VIRTIS performed limb scans of the OH Meinel $\Delta v = 1,2$ rotational-vibrational bands from 87 to 105 km covering the latitude range from 38 to 47°N. Only the relative OH(v) population distribution of OH(v = 1–9) was derived in this study. The Scanning Imaging Absorption spectroMeter for Atmospheric CHartographY (SCIAMACHY) instrument on the Envisat mission measured several OH emissions from 240 to 2,380 nm, among them 9–6, 8–5, 8–3, 5–2, 4–2, and 3–1 rotational-vibrational bands. Zhu et al. (2020) used these SCIAMACHY observations to retrieve OH($v = 4, 5, 8, 9$) number densities. The Sounding of the Atmosphere using Broadband Emission Radiometry (SABER) instrument on the TIMED mission measures nighttime emissions of the OH Meinel bands at 2.0 and 1.6 μm originating from $v = 8$, 9 and 4, 5, respectively. The 2.0 μm emission was used by Mast et al. (2013) to obtain sum of number densities for OH($v = 8$) and OH($v = 9$) in the mesosphere. Overall, with the exception of a few studies which derive specific OH(v) number densities, there have been no reported retrievals of total nighttime [OH] in the mesosphere and lower thermosphere (MLT) important for validating nighttime chemical models of these atmospheric layers.

The brief overview for a selected but not comprehensive list of studies which is given above presents the current status of the specific OH vibrational level densities retrievals from the OH emissions. In our study, we present a novel approach for simultaneous self-consistent retrieval of [$O(^3P)$] and [OH], where [OH] is the total OH number density which is the sum of both ground and excited vibrational state populations, in the MLT using nighttime satellite observations of OH band emissions. We apply this technique to the SABER 2.0 and 1.6 μm channel signals, which measure the OH(9-7) + OH(8-6) and OH(5-3) + OH(4-2) Meinel bands, respectively, as well as to SCHIAMACHY measured OH(9-6), OH(8-5), OH(5-2), and OH(4-2) band emissions. We show first retrieval results using both instruments and compare retrieved [$O(^3P)$] and [OH] to those simulated by the Whole Atmosphere Community Climate Model (WACCM; Gettelman et al., 2019).

2. Non-Local Thermodynamic Equilibrium Model

We apply the non-local thermodynamic equilibrium (non-LTE) model for OH(v) developed by Panka et al. (2017). This model is the first one which incorporated the new multiquantum quenching process OH(v) + $O(^3P)$ (R5 in Table 1 below) suggested by Sharma et al. (2015) and confirmed via experimental studies by Kalogerakis et al. (2016). Accounting for this new process allows our model for the first time to reproduce the strong 4.3 μm nighttime emission measured by SABER. It was shown that this emission is pumped by the energy transfer chain OH(v) ⇒ $O(^1D)$ ⇒ $N_2(v)$ ⇒ $CO_2(v_3)$. Further, this model in combination with a new retrieval approach which utilized both SABER OH channels led to revised nighttime atomic oxygen retrieved from the SABER OH emissions (Panka et al., 2018). Here we provide updates of the Panka et al. (2017) model as well as discuss its features which are important for the new technique of simultaneous [$O(^3P)$] and [OH] retrievals from the OH band emissions.

Following Panka et al. (2017), our current model accounts for 10 vibrational levels with $v = 0$–9. Collisional relaxation processes as well as chemical reactions accounted for in the model with corresponding rate coefficients are given in the Table 1. It solves the system,

$$\sum_{v'} R_{vv'} n_{v'} = f_v P_{\mathrm{OH}}, \tag{1}$$

where $R_{vv'}$ for $v \neq v'$ are sums of rates for various radiative and collisional transitions between level v and v', ($R_{vv'} = -R_{v'v}$) whereas R_{vv} is the sum (taken with the minus sign) of all nondiagonal elements in the v column of the matrix R plus the term $k_7(v)[O(^3P)]$, which is the chemical removal rate of the OH(v) state in reaction OH(v) + $O(^3P)$ (R7 in Table 1). Further, $n_v = [\mathrm{OH}(v)]$ is the density or population of vibrational level v and the right side of Equation 1 are chemical production terms, with the total OH production rate P_{OH} and branching ratios f_v. Equation 1 is equivalent to the traditional presentation of the OH(v) non-LTE problem $n_v L_v = P_v$ (see, for instance, Grygalashvyly et al. (2014)) in terms of total production P_v and loss L_v

Table 1
Chemical and Collisional Processes Used in the Model

	Reaction	Reaction rate (cm^3sec^{-1})	Reference
(R1)	$H + O_3 \rightarrow OH(v \le 9) + O_2$	$k_1 = {}^{a}f_v^{(1)} \times 1.4 \times 10^{-10}\exp(-470/T)$	Burkholder et al. (2015) & Adler-Golden (1997)
(R2)	$HO_2 + O(^3P) \rightarrow OH + O_2$	$k_2 = {}^{b}f_v^{(2)} \times 3.0 \times 10^{-11}\exp(200/T)$	Burkholder et al. (2015)
(R3)	$OH(v \le 9) + N_2(0) \leftrightarrow OH(v\text{-}1) + N_2(1)$	$k_3 = {}^{c}f_v^{(3)} \times 1.4 \times 10^{-13}$	Adler-Golden (1997) & Lacoursière et al. (2003)
(R4)	$OH(v \le 9) + O_2(0) \leftrightarrow OH(0 \le v' \le v\text{-}1) + O_2(1)$	$k_4 = {}^{d}f_v^{(4)} \times 10^{-13}$	Adler-Golden (1997)
(R5)	$OH(v \ge 5) + O(^3P) \leftrightarrow OH(0 \le v' \le v\text{-}5) + O(^1D)$	$k_5 = {}^{e}f_v^{(5)} \times (2.3 \pm 1) \times 10^{-10}$	Kalogerakis et al. (2016) & Sharma et al. (2015)
(R6)	$OH(v \le 9) + O(^3P) \leftrightarrow OH(0 \le v' \le v\text{-}1) + O(^3P)$	see text	Caridade et al. (2013)
(R7)	$OH(v \le 9) + O(^3P) \rightarrow H + O_2$	$k_7 = 4.5 \times 10^{-11}$, see text	Caridade et al. (2013)

${}^{a}f_v^{(1)}(v = 5\text{–}9) = (0.01, 0.03, 0.15, 0.34, 0.47)$. ${}^{b}f_v^{(2)}(v = 0\text{–}9)$ see text. ${}^{c}f_v^{(3)}(v = 1\text{–}9) = (0.06, 0.10, 0.17, 0.30, 0.52, 0.91, 1.6, 7, 4.8)$. ${}^{d}f_v^{(4)}(v = 1\text{–}9) = (1.9, 4, 7.7, 13, 25, 43, 102, 119, 309)$. ${}^{e}f_v^{(5)}(v = 5\text{–}9) = (0.91, 0.61, 0.74, 0.87, 1.0)$.

rates for each v, where in our notations $P_v = f_v P_{OH} + \sum_{v' \neq v} R_{v'v} n_{v'}$ and $L_v = R_{vv}$. However, Equation 1 is more convenient for further analysis.

In the nighttime MLT, hydroxyl is mainly produced in two reactions (Brasseur & Solomon, 2006):

$$H + O_3 \rightarrow OH + O_2 \tag{R1}$$

and

$$HO_2 + O(^3P) \rightarrow OH + O_2, \tag{R2}$$

(reactions R1 and R2 in Table 1) with production rates

$$P_1 = k_1[H][O_3] \quad \text{and} \quad P_2 = k_2[HO_2][O(^3P)], \tag{2}$$

respectively. As a result

$$P_{OH} = P_1 + P_2 = P_{OH}(F_1 + F_2), \tag{3}$$

where $F_1 = P_1/P_{OH}$ and $F_2 = P_2/P_{OH}$ are relative contributions of each reaction to the total production. With accounting for the normalized branching ratios $f_v^{(1)}$ and $f_v^{(2)}$ ($\sum_v f_v^{(1,2)} = 1$) for reactions (R1) and (R2), respectively, f_v in the right hand side of Equation 1 is

$$f_v = f_v^{(1)} F_1 + f_v^{(2)} F_2, \tag{4}$$

where, again, $\sum_v f_v = 1$.

The relative contributions $F_1(z)$ and $F_2(z)$ of each OH chemical production reaction are determined from simulations using version 6 of WACCM (Gettelman et al., 2019) run with specified dynamics. In this configuration the dynamical fields (temperature, zonal and meridional winds and surface pressure) are constrained in the troposphere and stratosphere to follow the Modern Era Retrospective Analysis for Research and Applications (Molod et al., 2015). Using WACCM [H], [O_3], [HO_2], and [$O(^3P)$] throughout the year, we find that reaction (R2) contributes to the overall OH production below 87 km, while reaction (R1) completely dominates above this altitude. Accounting for reaction (R2) in the current model differs from the one described by Panka et al. (2017), however, it does not change its main properties. We show below that this modification is important for retrieving [OH] in the lower MLT and has only a minor effect on the [$O(^3P)$] retrievals presented by Panka et al. (2018).

Other chemical production and loss reactions, such as $H + HO_2$ and $OH + HO_2$, may impact the OH balance in the mesosphere (Brasseur & Solomon, 2006). Using WACCM simulations, we find, however, that between

80 and 100 km, these reactions contribute less than 1% to the total [OH] in a majority of cases. In a small number of cases the H + HO_2 reaction contributes at most only 5% of the total [OH] at 80 km, whereas above this altitude contributions are still negligible. Therefore, we ignore these reactions in our retrievals as they do not change the retrieved [OH].

Reaction (R1) is known to produce vibrationally excited OH(v) from v = 5–9 (Adler-Golden, 1997; Klenerman & Smith, 1987; Ohoyama et al., 1985). Branching ratios for this reaction in Table 1, $f_v^{(1)}$, are taken from Adler-Golden (1997) while previous studies also have concluded similar initial OH(v) distributions.

In contrast to (R1), the initial vibrational excitation of OH produced in the reaction (R2), where OH(v) levels from v = 0–6 are energetically accessible, is not well understood. Although Lunt et al. (1988) reported laboratory evidence that OH produced in this reaction was vibrationally excited, the branching ratios were not measured. In the same year, analyzing laboratory data, Kaye (1988), suggested OH is vibrationally excited from v = 3–6. Llewellyn and Solheim (1978) as well as McDade and Llewellyn (1987) assumed, nevertheless, in their studies of atmospheric airglow observations that this reaction does not produce vibrational excited OH at all. On the other hand, Lopez-Moreno et al. (1987) in a similar study supposed OH is vibrationally excited from v = 3–6, whereas Makhlouf et al. (1995) in their theoretical model of the OH emission fluctuations assumed OH is excited only from v = 0–3. It is also worth noting that all laboratory studies and airglow modeling efforts outlined above did not account for the reaction OH(v) + O(^{3}P) recently found by Sharma et al. (2015) and Kalogerakis et al. (2016) (Reaction [R5] in Table 1). Due to this lack of laboratory and theoretical data on the HO_2 + O(^{3}P) reaction, we consider in this study four different cases of its OH production, which are described in detail in Section 4.

We applied the rate coefficients k_3 for the reaction (R3) OH(v) + N_2(0) which are increased by a factor of 1.4 compared to those of Adler-Golden (1997), as was suggested by López-Puertas et al. (2004) for low MLT temperatures, supported by Lacoursière et al. (2003) and by Burtt and Sharma (2008). These k_3 values are close but not equal to those calculated by Burtt and Sharma (2008). We, however, performed a test run using exactly k_3 data from Burtt and Sharma (2008). The difference of retrieved results (O(^3P) and total OH densities) did not exceed 3%.

We consider in Table 1 two energy transfer processes and one chemical reaction for OH(v) + O(^{3}P) collisions: vibrational-electronic (R5) and vibrational-translational (R6) transfers, and chemical removal (R7). Multiquantum quenching is assumed for both reactions R5 and R6 with the coefficients for R5 taken from Kalogerakis et al. (2016) and with those for R6 taken from Table 1 of Caridade et al. (2013). Caridade et al. (2013) suggested a rate coefficient $k_7(v)$ for reaction R7 which increases with increasing v. We show the mean value of this coefficient k_7 in Table 1 which is introduced in Section 3.

We also make another change to our OH non-LTE model from the previous studies, namely we removed the 1.18 factor from the quenching rate coefficient between OH(v) + O_2. This factor results in a slightly higher quenching rate than the associated experimental studies reported, which have been nicely summarized in Xu et al. (2012). We find that reducing OH(v) + O_2 quenching rate has minor effects on the atomic oxygen densities (2%–3%) compared to those retrieved by Panka et al. (2018).

3. Retrieval Algorithm

We use SABER measurements as the example for the description of the algorithm, however, any instrument which observes multiple OH rotational-vibrational emissions simultaneously can utilize this methodology. SABER measures the OH Meinel band emissions in two near-infrared channels: channel 8 at 2.0 μm (9→7 and 8→6 bands), and channel 9 at 1.6 μm (5→3 and 4→2 bands). Volume emission rates (VER) for each channel can be presented as:

$$\mathrm{VER} = [\mathrm{OH}]\sum_v A_{v,v'} p_v, \tag{5}$$

where $A_{v,v'}$ are the Einstein coefficients for bands contributing to measured emission and $p_v = n_v/[\mathrm{OH}]$ ($\sum_v p_v = 1$) are normalized populations of vibrational levels. Following Equation 5, the ratio $\mathrm{VER}^{Ch8}/\mathrm{VER}^{Ch9}$ for channels 8 and 9 can be reduced to the ratio of sums $\sum_v A_{v,v'} p_v$ and is, therefore, independent of [OH]. On

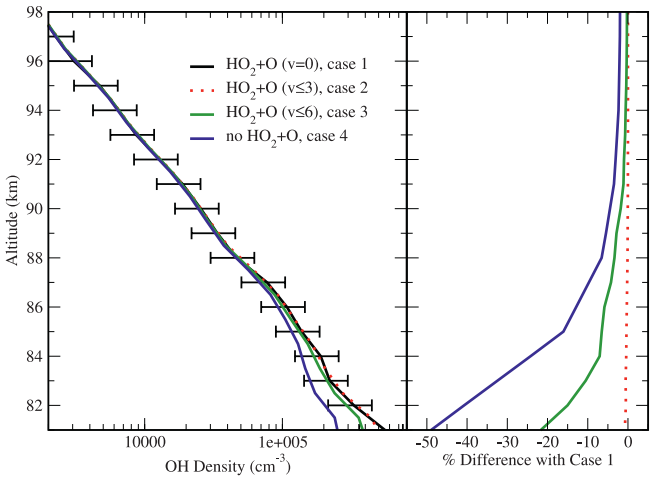


Figure 1. Retrieved [OH] profiles using SABER observations for four reaction (R2) production cases. See text for details. SABER, Sounding of the Atmosphere using Broadband Emission Radiometry.

the other hand, it follows from Equation 1 that normalized populations p_v satisfy the same system where P_{OH} is replaced by the production of OH per sec per one OH molecule $\Pi_{OH} = P_{OH}/[OH]$. This ratio depends on the collisional quenching rates and chemical loss rates which comprise the $R_{vv'}$ coefficients of Equation 1. The latter makes the volume emission rate ratios dependent on the densities of the collisional partners of OH (N_2, O_2, and $O(^3P)$) which are involved in its vibrational relaxation and chemical removal. Panka et al. (2018) found that VER^{Ch8}/VER^{Ch9} are nearly linearly dependent on the atomic oxygen volume mixing ratio (VMR). By taking advantage of this relationship, a simple retrieval scheme was developed, which fits the VER ratio of the measured signals with the calculated ratio using the local $O(^3P)$ VMR as a fitting parameter. The obtained results were in good agreement with other atomic oxygen retrievals which used different instruments and methods.

After $[O(^3P)]$ has been retrieved from the VER ratios, the second step is retrieving [OH]. It follows from Equation 5, that if the normalized populations p_i are known, [OH] can be obtained by fitting the measured VER in any of the two SABER channels with this expression. However, Equation 1 suggests that to obtain p_i one needs to know both $[O(^3P)]$ (which enters the matrix coefficients $R_{vv'}$) and the production rate per one OH molecule $\Pi_{OH} = P_{OH}/[OH]$. On the other hand, since radiative and collisional transitions between vibrational levels do not change total [OH], the sum of Equation 1 over $v = 0$–9 reduces to $L_{OH} = [O(^3P)]\sum_v k_7(v)$ $n_v = P_{OH}$ or to $L_{OH} = k_7[O(^3P)][OH] = P_{OH}$ with $k_7 = \sum_v k_7(v)p_v$, where L_{OH} is the total chemical loss of OH. This expresses the balance between chemical loss and production of OH in the reactions accounted in the model which is built in into system (1). Therefore, if following this balance relation, we replace P_{OH} in Equation 1 by its total loss L_{OH} then this will not change the solution of Equation 1. As a result, the retrieved [OH] is

$$[OH]^{retr} = \frac{VER^{mes}}{\sum_{v'} A_{v,v'} p_v^*}, \tag{6}$$

where VER^{mes} is the measured VER in any of two SABER channels and p_v^* are normalized populations obtained from solving Equation 1 for $\Pi_{OH} = k_7[O(^3P)]^{retr}$, where $[O(^3P)]^{retr}$ is the $[O(^3P)]$ retrieved from VER ratios at the previous step in the algorithm. We note here that in the calculations described below, k_7 varied slightly around the value of 4.5×10^{-11} cm^3 sec^{-1} which we show in Table 1. Additionally, replacing $k_7(v)$ of Caridade et al. (2013) with this constant value influences neither $[O(^3P)]$ nor [OH] retrievals discussed below.

4. The Role of Reaction R2

Due to a lack of laboratory and theoretical data on the OH(v) produced in the $HO_2 + O(^3P)$ reaction, we examined four cases: (1) no OH vibrational excitation, or $f_0^{(2)} = 1.0$, $f_v^{(2)} = 0$ for $v = 3$–9; (2) OH is excited up to v = 3, where we assume uniform branching ratios from v = 0–3; (3) OH is excited up to v = 6, where we use Adler-Golden (1997) branching ratios for excitation from OH(v = 1–6); as well as the case (4) no reaction (R2), or $P_2 = 0$.

The [OH] profiles retrieved using the two-channel algorithm, which is described in the previous section, from the SABER channel 8 and 9 VERs for four cases of reaction (R2) production are plotted in the left panel of Figure 1, while differences between cases 2–4 compared to case 1 are shown in the right panel of this figure. The black solid curve represents case 1, where we assume no OH vibrational excitation in reaction (R2), and includes a 35% (see Section 5) uncertainty range. The red dotted and green solid profiles represent [OH] retrievals for case 2 and 3, respectively. Case 2 brings almost no difference in the retrieved [OH] profiles compared to case 1. The lower vibrational levels OH(0–3) produced in this case of do not significantly contribute to the emission of bands with upper levels OH(4–9) used in this tests. This is not true for case 3.

As a result, the case 3 pumping scheme decreases the [OH] profile compared to case 1 by roughly 10%–20% below 84 km. However, above this altitude the case 3 pumping scheme has almost no impact due to the decreasing contribution with altitude of reaction (R2) to the total OH production. This alternative branching ratio distribution for reaction (R2) also increased [$O(^3P)$] retrievals (not shown) by 10% below 84 km. Overall, both branching ratio distributions used for case 2 and 3 do not change the [$O(^3P)$] and [OH] profiles to a large degree compared to the original case 1 set up (OH($v = 0$)), especially considering all 3 cases fall within the uncertainty range. Lastly, we also tested the case where reaction (R2) is not considered at all (case 4, blue solid). In the upper mesosphere, where this reaction has little impact on the OH production, the [OH] retrievals for this case look similar to cases 1–3. In the lower mesosphere, however, the importance of reaction (R2) becomes clear, as differences between case 4 and cases 1–3 reach up to 50%. This further demonstrates the importance of considering reaction (R2) when retrieving [OH]. Since cases 1–3 all fall within the uncertainty range of case 1, we use the case 1 model to retrieve [$O(^3P)$]/[OH] presented in Section 5.

5. Results and Discussion

We apply the simultaneous [$O(^3P)$]/[OH] retrieval technique described in Section 3 to SABER and SCIAMACHY VER measurements from 80 to 97 km. Model inputs such as temperature/pressure and measured VERs are taken from the publicly available SABER Level 2A data set, while [O_2], [N_2], as well as initial guesses for [$O(^3P)$] are taken from WACCM. SCIAMACHY measured VERs are taken from the publicly available Level 1b Version 8 data set. In the case of SCIAMACHY we first substituted SCIAMACHY OH(9-6), OH(8-5), OH(5-2), and OH(4-2) Einstein coefficients into Equation 5 and found that the ratios of SCIAMACHY VERs and atomic oxygen also demonstrate near linear dependence, similar to the VER ratios of SABER observation studied by Panka et al. (2018).

We performed an extensive error analysis on the retrieved products which are described in detail in Panka (2017). The 1-σ uncertainty of [$O(^3P]$ and [OH] were determined by considering (1) the random error, which gives a measure of the imprecision, specifically the random noise of the radiometer instrument (i.e SABER and SCIAMACHY), and (2) the systematic error, which provides information on the inaccuracy or the bias of the inferred quantities. The important sources of the systematic errors are instrument calibrations, non-LTE modeling parameters such as rate coefficients, and assumed atmospheric input parameters (temperature/pressure and densities of molecules). We found that, overall, for altitudes above 85 km, the systematic sources dominate the contribution to the total uncertainty, specifically quenching of OH by O_2 and $O(^3P)$. Above 85 km, the combined 1-σ error for [$O(^3P)$] was estimated to be ~25%, while for [OH] it was ~35% for both SABER and SCIAMACHY retrievals.

Figure 2 displays retrieved mean [$O(^3P)$] and [OH] for latitude regions 20–40°N (left-panels) and 40–60°N (right-panels) for September 2005. For each instrument, we performed retrievals using three sets of OH Einstein coefficients: Groenenboom (2007) (VDL), Brooke et al. (2016) (BROOKE), and Gordon et al. (2017) (HITRAN). We also plot [$O(^3P)$]/[OH] WACCM calculations based on Gettelman et al. (2019) as well as recent [$O(^3P)$] results of Zhu and Kaufmann (2018) and Zhu and Kaufmann (2019) derived from other SCIAMACHY emission bands. The red profiles represent [$O(^3P)$]/[OH] retrievals using SABER signals, while the blue profiles are retrieved from SCIAMACHY (for which we will use SCIA as shorthand hereafter). The blue and red profiles with triangles (SCIA-HITRAN and SABER-HITRAN) are the only ones plotted with error bars of ±25% for presentation purposes, however, all [$O(^3P)$]/[OH] retrievals share the same uncertainty. This uncertainty is estimated for SABER and SCIA [$O(^3P)$] retrievals as described above.

Panka et al. (2018) were first to demonstrate that accounting for the new OH(v) + $O(^3P)$ (R5 in Table 1) multiquantum process brought [$O(^3P)$] retrieved from SABER measurements in agreement to other independent observations. All six retrieved [$O(^3P)$] vertical profiles presented in Figure 2 overlap within their uncertainties. They also provide an important proof of our OH(v) relaxation model and our retrieval technique. The results obtained from observations of different Meinel band emissions by two different instruments demonstrate excellent agreement, as well as to [$O(^3P)$] derived from observations of other emissions.

We note, however, that the SABER-HITRAN profiles in Figure 2 demonstrate the highest values of [$O(^3P)$] retrieved in this study and lie outside the tight bands that the other five curves build. The SABER-BROOKE (red-square) and SABER-VDL (red-circle) [$O(^3P)$] profiles are similar in density to one another and to

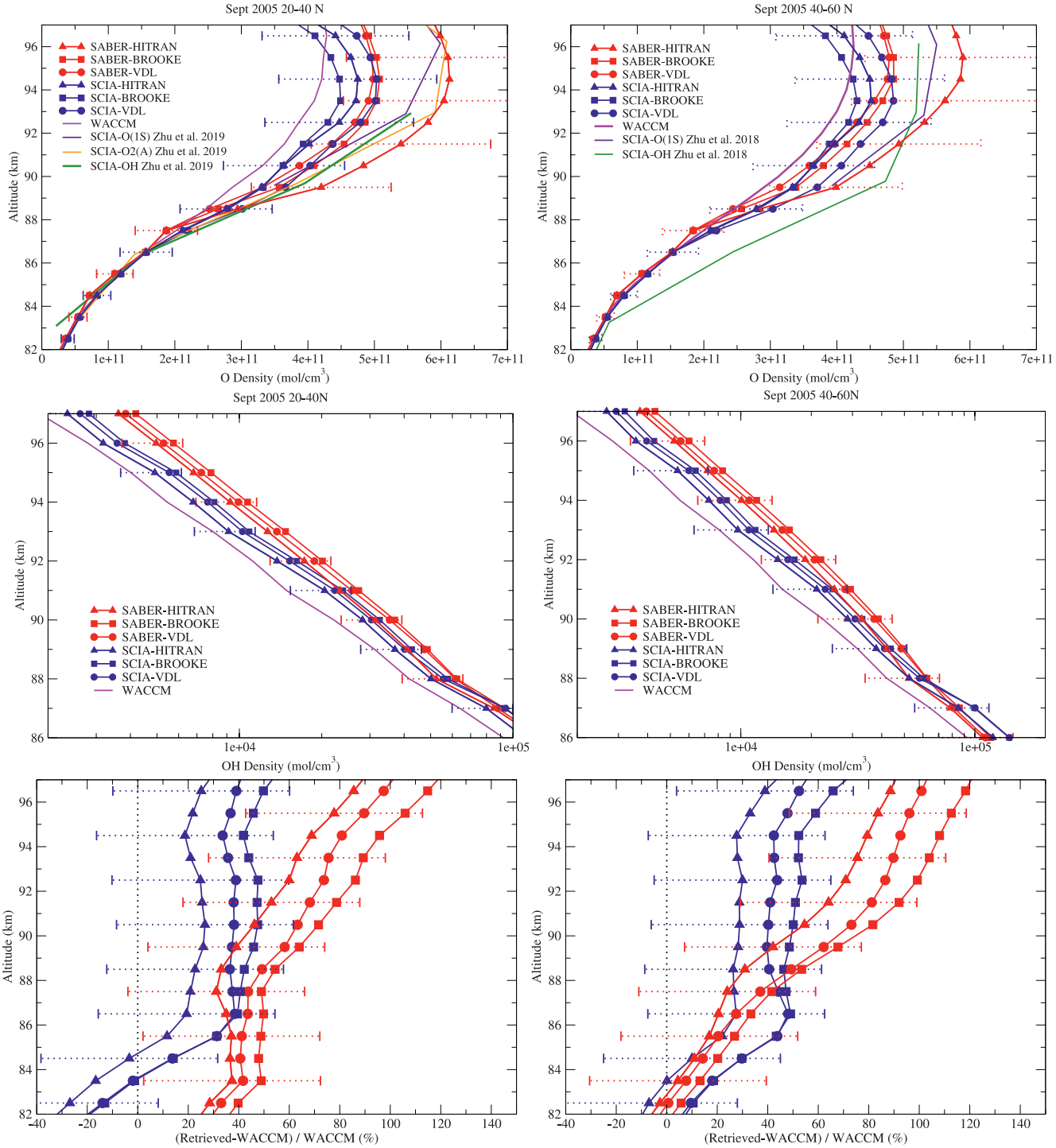


Figure 2. Zonal monthly mean profiles of the retrieved O(^{3}P) and OH density from 20 to 40°N (left-panels) and 40–60°N (right panels) for the month of September 2005. Top panel: retrieved O(^{3}P) density. Middle-panel: retrieved OH densities. Bottom panel: OH densities residuals with respect to WACCM simulations. See text for descriptions of the individual profiles.

three SCIA profiles but show pronounced differences compared to SABER-HITRAN profile. The higher SABER-HITRAN [O(^{3}P)] can be attributed to differences of the HITRAN A-coefficients for SABER measured Meinel bands compared to those from two other A-sets as they are the only varying parameters among the SABER [O(^{3}P)] retrieval runs. We otherwise use the same atmospheric input, collisional rates, reactions

and measured signals. We note also, that SABER-HITRAN [O(^{3}P)] is the closest to the SCIA results, obtained from other emissions as well as to the latest SCIA OH(v) emissions result. The SCIA [O(^{3}P)] profiles on the other hand are all similar to each other and are closest in density to WACCM (magenta) calculation, specifically above 90 km. The Einstein coefficients among these data-sets vary significantly by up to 50% for some transitions, however, the combination of bands that we are analyzing for this study suppress large differences in their radiative rates. The results of Zhu and Kaufmann (2018) and Zhu and Kaufmann (2019) are consistent with SCIA and SABER [O(^{3}P)] profile from this study up to 92 km and are in slightly better agreement with SABER-HITRAN above this altitude.

The middle panels of Figure 2 show [OH] from SABER and SCIA observations, which are retrieved at step 2 of the algorithm described in Section 3. Similar to the top panels, only error bars for the SCIA-HITRAN and SABER-HITRAN profile are displayed with an uncertainty of ±35%. We find for these retrievals, that, on average, the OH ground state population OH(0) accounts for 99%, 82%, 58%, and 53% of the OH molecules at 80, 85, 90, and 95 km, respectively.

The bottom panels of Figure 2 show the residuals between retrieved [OH] and WACCM [OH]. We find that SCIA [OH], for all three sets of Einstein coefficients, are in relatively good agreement with WACCM [OH] (i.e., within 20%–50%). The SCIA-HITRAN [OH] are in the best agreement, with densities only 20%–30% higher than WACCM, while SCIA-BROOKE [OH] was larger than WACCM by 40%–50% above 86 km. When the uncertainty range of ±35% is considered, the SCIA [OH] profiles do not differ significantly from WACCM.

The SABER [OH] profiles are in very good agreement with SCIA [OH] from 85 to 90 km. Above this altitude SABER [OH] are higher than WACCM and SCIA, reaching differences up to 60%–100% and 50%–60%, respectively. The SABER [OH] differences above 90 km also become larger with altitude, whereas SCIA [OH] profiles keep a relatively uniform difference from WACCM above 86 km. While the SABER-BROOKE and SABER-VDL [OH] retrievals produce the highest [OH], their [O(^{3}P)] counterparts are generally in good agreement with one another and with SCIA and WACCM [O(^{3}P)]. SABER-BROOKE and SCIA-BROOKE cases also lead to retrievals that have similar [O(^{3}P)] while the SABER-BROOKE [OH] are larger than SCIA-BROOKE by up to 60% above 90 km. This same behavior is seen for SABER-VDL (red-circle) and SCIA-VDL (blue-circles) cases suggesting that there are intrinsic discrepancies between SABER and SCIA observations as all other parameters in these retrievals are identical.

This discrepancy between SABER and SCIA data was first reported by Zhu et al. (2020). The authors used SCIA signals at OH(9-6), OH(8-5), OH(5-2), and OH(4-2) to retrieve OH(v = 4, 5, 8, and 9), then subsequently simulate SABER OH 1.6 and 2.0 μm VERs in range of 80–96 km. The authors found SABER OH in-band VERs measurements at 2.0 and 1.6 μm to be 35% and 23% higher than corresponding simulations obtained from SCIA OH data, respectively, if all altitudes and latitudes are considered simultaneously in one fit. Particularly for mid-latitude regions, the study found SABER OH VERs to be higher than SCIA ones in a range of 21%–50% at 83 km and 28%–100% at 96 km. These reported differences increase with altitude and are of similar magnitude to [OH] retrieval differences displayed in the middle and bottom panels of Figure 2. Zhu et al. (2020) further reports that the signal differences can be mostly reduced by up to 50% by taking into account uncertainties in the Einstein coefficients as well as model parameter uncertainties and radiometric calibration. The bottom panels of Figure 2 already demonstrate the effects of Einstein coefficients on [OH] retrieval obtained using our technique, which utilizes SCIA VERs directly and does not involve Einstein coefficient ratios required for simulating SABER data. Meanwhile, taking into account the [OH] uncertainty of ±35% allows for the SABER and SCIA [OH] retrievals to overlap even in the upper altitude region where differences are no larger than 60%.

6. Conclusion

A new technique for the simultaneous self-consistent retrieval of [O(^{3}P)] and [OH] from space observations of OH Meinel band emissions is presented. The new method significantly differs from techniques used in previous studies by Good (1976), Mlynczak et al. (2013), Kaufmann et al. (2014), Mlynczak et al. (2018), Zhu and Kaufmann (2018), and Fytterer et al. (2019). By operating with ratios of VERs of two different OH bands (or combination of bands), this method first retrieves [O(^{3}P)] without a priori knowledge of [OH].

It also does not require knowledge of the total OH chemical production rate and does not involve the assumption of chemical balance between the ozone loss and production, used in previous studies. Then using retrieved [$O(^3P)$], this method exploits the chemical balance between OH production and loss and retrieves [OH] by fitting VER in any of two simultaneously observed OH emission bands (or band combinations).

We apply the new retrieval technique and revised OH non-LTE model for simultaneous retrievals of [$O(^3P)$]/[OH] from the OH limb emissions measured by the SABER and SCHIAMACHY instruments. We perform detailed comparisons of [$O(^3P)$]/[OH] retrievals from observations of both instruments as well as with WACCM calculations. We find that [$O(^3P)$] demonstrate low sensitivity to the variation of Einstein A-coefficients for bands used in this analysis and are almost all in good agreement with one another from 80-96 km (with an exception for A-coefficients taken from current HITRAN database). Similar results are seen for the retrieved [OH] below 90 km. Above this altitude, however, the same retrieval method applied to SCIAMACHY and SABER yield rather different [OH]. The SABER retrieved [OH] are higher than SCIAMACHY, reaching differences up to 50%–60%, however, these differences are mostly suppressed when accounting for model parameter uncertainties and signal noise. SCIAMACHY retrieved [OH] is generally in good agreement with WACCM after accounting for uncertainties, while SABER [OH] is larger than WACCM by up to a factor of 2. These discrepancies require further investigation.

The new retrieval method developed in this study can be applied to retrieving both [$O(^3P)$] and [OH] from any other instrument observations of nighttime OH airglows, which simultaneously measure at least two different OH bands. For instance the method can be used for OSIRIS (Sheese et al., 2014) (Optical Spectrograph and Infrared Imaging System) observations which measures various OH Meinel band emissions in broad spectral intervals.

Data Availability Statement

The WACCM data used in this study can be obtained at the National Center for Atmospheric Research website: https://www.earthsystemgrid.org/. The SCIAMACHY Level1b Version 8 data used in this study are available at http://www.sciamachy.org/products/index.php. SABER Version 2A data are available at http://saber.gats-inc.com. Retrievals of SABER $O(^3P)$ and OH densities are available on the NASA Space Physics Data Facility (SPDF): https://spdf.gsfc.nasa.gov/ and the SABER public site: http://saber.gats-inc.com/.

Acknowledgments
The work by Peter A. Panka was supported by an appointment to the NASA Postdoctoral Program at Goddard Space Flight Center, administered by USRA through contract with NASA. The work by Alexander A. Kutepov was supported by the NSF grant 1301762 and the NASA grant NNX15AN08G. The work by Konstantinos S. Kalogerakis was supported by NSF grant AGS-1441896 and NASA grant 80NSSC17K0638. The work by Diego Janches was supported by the NASA/TIMED project. The work by Y. Zhu was supported by the Specialized Research Fund for State Key Laboratories and NSSC Research Fund for key development directions.

References

Adler-Golden, S. (1997). Kinetic parameters for OH nightglow modeling consistent with recent laboratory measurements. *Journal of Geophysical Research*, *102*(A9), 19969–19976. https://doi.org/10.1029/97JA01622

Brasseur, G. P., & Solomon, S. (2006). *Aeronomy of the middle atmosphere: Chemistry and physics of the stratosphere and mesosphere* (Vol. 32). Dordrecht, Netherlands: Springer Science & Business Media.

Brooke, J. S., Bernath, P. F., Western, C. M., Sneden, C., Afşar, M., Li, G., & Gordon, I. E. (2016). Line strengths of rovibrational and rotational transitions in the $X^2\Pi$ ground state of OH. *Journal of Quantitative Spectroscopy and Radiative Transfer*, *168*, 142–157.

Burkholder, J., Sander, S., Abbatt, J., Barker, J., Huie, R., Kolb, C., & Wine, P. (2015). *Chemical kinetics and photochemical data for use in atmospheric studies: Evaluation number 18*. JPL TRS 1992. Pasadena, CA: Jet Propulsion Laboratory, National Aeronautics and Space Administration.

Burtt, K. D., & Sharma, R. D. (2008). Near-resonant energy transfer from highly vibrationally excited OH to N_2. *The Journal of Chemical Physics*, *128*(12), 124311.

Caridade, P. J. S. B., Horta, J.-Z. J., & Varandas, A. J. C. (2013). Implications of the O + OH reaction in hydroxyl nightglow modeling. *Atmospheric Chemistry and Physics*, *13*(1), 1–13.

Cosby, P., & Slanger, T. (2007). OH spectroscopy and chemistry investigated with astronomical sky spectra. *Canadian Journal of Physics*, *85*(2), 77–99.

Fytterer, T., von Savigny, C., Mlynczak, M., & Sinnhuber, M. (2019). Model results of oh airglow considering four different wavelength regions to derive night-time atomic oxygen and atomic hydrogen in the mesopause region. *Atmospheric Chemistry and Physics*, *19*(3), 1835–1851.

Gettelman, A., Mills, M., Kinnison, D., Garcia, R., Smith, A., Marsh, D., et al. (2019). The Whole atmosphere community climate model version 6 (WACCM6). *Journal of Geophysical Research: Atmospheres*, *124*(23), 12380–12403. https://doi.org/10.1029/2019JD030943

Good, R. E. (1976). Determination of atomic oxygen density from rocket borne measurement of hydroxyl airglow. *Planetary and Space Science*, *24*(4), 389–395.

Gordon, I. E., Rothman, L. S., Hill, C., Kochanov, R. V., Tan, Y., Bernath, P. F., et al. (2017). The HITRAN2016 molecular spectroscopic database. *Journal of Quantitative Spectroscopy and Radiative Transfer*, *203*, 3–69.

Grygalashvyly, M., Sonnemann, G., Lübken, F.-J., Hartogh, P., & Berger, U. (2014). Hydroxyl layer: Mean state and trends at midlatitudes. *Journal of Geophysical Research: Atmospheres*, *119*(21), 12391–12419. https://doi.org/10.1002/2014jd022094.

Kalogerakis, K. S. (2019). A previously unrecognized source of the O_2 atmospheric band emission in earth's nightglow. *Science Advances*, *5*(3), eaau9255.

Kalogerakis, K. S., Matsiev, D., Sharma, R. D., & Wintersteiner, P. P. (2016). Resolving the mesospheric nighttime 4.3 μm emission puzzle: Laboratory demonstration of new mechanism for OH(υ) relaxation. *Geophysical Research Letters*, *43*(17), 8835–8843. https://doi.org/10.1002/2016GL069645

Kaufmann, M., Zhu, Y., Ern, M., & Riese, M. (2014). Global distribution of atomic oxygen in the mesopause region as derived from SCIAMACHY O(^{1}S) green line measurements. *Geophysical Research Letters*, *41*(17), 6274–6280. https://doi.org/10.1002/2014gl060574

Kaye, J. A. (1988). On the possible role of the reaction O + HO_2 → OH + O_2 in OH airglow. *Journal of Geophysical Research*, *93*(A1), 285–288.

Klenerman, D., & Smith, I. W. (1987). Infrared chemiluminescence studies using a SISAM spectrometer. Reactions producing vibrationally excited OH. *Journal of the Chemical Society, Faraday Transactions 2: Molecular and Chemical Physics*, *83*(1), 229–241.

Lacoursière, J., Dyer, M. J., & Copeland, R. A. (2003). Temperature dependence of the collisional energy transfer of OH(v = 10) between 220 and 310 K. *The Journal of Chemical Physics*, *118*(4), 1661–1666. https://doi.org/10.1063/1.1530581

Llewellyn, E., & Solheim, B. (1978). The excitation of the infrared atmospheric oxygen bands in the nightglow. *Planetary and Space Science*, *26*(6), 533–538.

Lopez-Moreno, J., Rodrigo, R., Moreno, F., Lopez-Puetas, M., & Molina, A. (1987). Altitude distribution of vibrationally excited states of atmospheric hydroxyl at levels v = 2 to v = 7. *Planetary and Space Science*, *35*(8), 1029–1038.

López-Puertas, M., Garcia-Comas, M., Funke, B., Picard, R. H., Winick, J. R., Wintersteiner, P. P., & Gordley, L. L. (2004). Evidence for an OH(ν) excitation mechanism of CO_2 4.3 μm nighttime emission from SABER/TIMED measurements. *Journal of Geophysical Research*, *109*, 2–15. https://doi.org/10.1029/2003JD004383

Lunt, S. T., Marston, G., & Wayne, R. P. (1988). Formation of O_2(a $^1\Delta_g$) and vibrationally excited OH in the reaction between O atoms and HO_x species. *Journal of the Chemical Society, Faraday Transactions 2: Molecular and Chemical Physics*, *84*(7), 899–912.

Makhlouf, U., Picard, R., & Winick, J. (1995). Photochemical-dynamical modeling of the measured response of airglow to gravity waves: 1. Basic model for OH airglow. *Journal of Geophysical Research*, *100*(D6), 11289–11311.

Mast, J., Mlynczak, M. G., Hunt, L. A., Marshall, B. T., Mertens, C. J., Russell, J. M., & Gordley, L. L. (2013). Absolute concentrations of highly vibrationally excited OH(υ = 9 + 8) in the mesopause region derived from the TIMED/SABER instrument. *Geophysical Research Letters*, *40*(3), 646–650. https://doi.org/10.1002/grl.50167

McDade, I., & Llewellyn, E. (1987). Kinetic parameters related to sources and sinks of vibrationally excited OH in the nightglow. *Journal of Geophysical Research*, *92*(A7), 7643–7650.

Migliorini, A., Gérard, J.-C., Soret, L., Piccioni, G., Capaccioni, F., Filacchione, G., & Tosi, F. (2015). Terrestrial OH nightglow measurements during the Rosetta flyby. *Geophysical Research Letters*, *42*(13), 5670–5677. https://doi.org/10.1002/2015gl064485

Mlynczak, M. G., Hunt, L. A., Mast, J. C., Thomas Marshall, B., Russell, J. M., Smith, A. K., & Gordley, L. L. (2013). Atomic oxygen in the mesosphere and lower thermosphere derived from SABER: Algorithm theoretical basis and measurement uncertainty. *Journal of Geophysical Research: Atmospheres*, *118*(11), 5724–5735. https://doi.org/10.1002/jgrd.50401

Mlynczak, M. G., Hunt, L. A., Russell, J. M., III, & Marshall, B. T. (2018). Updated SABER night atomic oxygen and implications for SABER ozone and atomic hydrogen. *Geophysical Research Letters*, *45*(11), 5735–5741. https://doi.org/10.1029/2018GL077377

Molod, A., Takacs, L., Suarez, M., & Bacmeister, J. (2015). Development of the GEOS-5 atmospheric general circulation model: Evolution from MERRA to MERRA2. *Geoscientific Model Development*, *8*(5), 1339.

Ohoyama, H., Kasai, T., Yoshimura, Y., Kimura, H., & Kuwata, K. (1985). Initial distribution of vibration of the OH radicals produced in the H + O_3 → OH($X^2\Pi_{1/2,3/2}$) + O_2 reaction. Chemiluminescence by a crossed beam technique. *Chemical Physics Letters*, *118*(3), 263–266.

Panka, P. A. (2017). *New non-LTE model of OH and CO2 emission in the mesosphere-lower thermosphere and its application to retrieving nighttime parameters* (PhD Dissertation). George Mason University. Retrieved from http://mars.gmu.edu/handle/1920/11272

Panka, P. A., Kutepov, A. A., Kalogerakis, K. S., Janches, D., Russell, J. M., Rezac, L., & Yiğit, E. (2017). Resolving the mesospheric nighttime 4.3 μm emission puzzle: Comparison of the CO_2(ν_3) and OH(ν) emission models. *Atmospheric Chemistry and Physics*, *17*(16), 9751–9760.

Panka, P. A., Kutepov, A. A., Rezac, L., Kalogerakis, K. S., Feofilov, A. G., Marsh, D., & Yiğit, E. (2018). Atomic oxygen retrieved from the SABER 2.0- and 1.6-μm radiances using new first-principles nighttime OH(ν) model. *Geophysical Research Letters*, *45*(11), 5798–5803. https://doi.org/10.1029/2018gl077677

Pickett, H., Read, W., Lee, K., & Yung, Y. (2006). Observation of night OH in the mesosphere. *Geophysical Research Letters*, *33*(19). https://doi.org/10.1029/2006gl026910

Sharma, R. D., Wintersteiner, P. P., & Kalogerakis, K. S. (2015). A new mechanism for OH vibrational relaxation leading to enhanced CO_2 emissions in the nocturnal mesosphere. *Geophysical Research Letters*, *42*, 4639–4647. https://doi.org/10.1002/2015GL063724

Sheese, P., Llewellyn, E., Gattinger, R., & Strong, K. (2014). OH Meinel band nightglow profiles from OSIRIS observations. *Journal of Geophysical Research: Atmospheres*, *119*(19), 11417–11428. https://doi.org/10.1002/2014jd021617

van der Loo, M. P., & Groenenboom, G. C. (2007). Theoretical transition probabilities for the OH Meinel system. *The Journal of Chemical Physics*, *126*(11), 114314.

Xu, J., Gao, H., Smith, A. K., & Zhu, Y. (2012). Using TIMED/SABER nightglow observations to investigate hydroxyl emission mechanisms in the mesopause region. *Journal of Geophysical Research*, *117*(D2), 1–22. https://doi.org/10.1029/2011JD016342

Zhu, Y., & Kaufmann, M. (2018). Atomic oxygen abundance retrieved from SCIAMACHY hydroxyl nightglow measurements. *Geophysical Research Letters*, *45*(17), 9314–9322. https://doi.org/10.1029/2018gl079259

Zhu, Y., & Kaufmann, M. (2019). Consistent nighttime atomic oxygen concentrations from O_2 A-band, O(^{1}S) green-line, and OH airglow measurements as performed by SCIAMACHY. *Geophysical Research Letters*, *46*(14), 8536–8545. https://doi.org/10.1029/2019gl083550

Zhu, Y., Kaufmann, M., Chen, Q., Xu, J., Gong, Q., Liu, J., & Riese, M. (2020). A comparison of OH nightglow volume emission rates as measured by SCIAMACHY and SABER. *Atmospheric Measurement Techniques*, *13*(6), 3033–3042.